Journal of MATERIALS RESEARCH

Article
DOI: 10.1557/jmr.2019.202

Solidification structure evolution of immiscible Al–Bi–Sn alloys at different cooling rates

Jinchuan Jie[1,a)], Zhilin Zheng[1], Shichao Liu[1], Shipeng Yue[1], Tingju Li[2]

[1]Key Laboratory of Solidification Control and Digital Preparation Technology (Liaoning Province), School of Materials Science and Engineering, Dalian University of Technology, Dalian 116024, China
[2]Laboratory of Special Processing of Raw Materials, School of Materials Science and Engineering, Dalian University of Technology, Dalian 116024, China
[a)]Address all correspondence to this author. e-mail: jiejc@dlut.edu.cn

Received: 5 March 2019; accepted: 29 May 2019

Under conventional solidification conditions, immiscible alloy melt would undergo large-scale composition segregation after liquid–liquid phase separation, resulting in the loss of properties and application value. In the present study, the ternary immiscible $Al_{70}Bi_{10}Sn_{20}$ alloy was chosen to study the effect of cooling rate on its resultant microstructure by casting the melt under different cooling conditions. The results indicated that the Al–Bi–Sn alloy with a slow cooling rate exhibits a strong spatial phase separation trend during solidification. However, as the cooling rate increases, the decreasing volume fraction of the segregated Bi–Sn-rich regions indicates the efficient suppression of spatial phase separation. The relatively dispersed distribution of Bi–Sn phase in the Al-rich matrix can be obtained by quenching the melt into water. The influence mechanism of cooling rate on the microstructure of the alloy is also discussed. The present study is beneficial to further tailoring the microstructure of immiscible alloys.

Introduction

Alloys with a miscibility gap in the liquid state are significant materials for a diversity of applications [1, 2, 3], such as welding materials, self-lubricating materials, and electrical contact materials. Al-based monotectic alloys are potential materials for the development of advanced self-lubricant bearings and solders [1, 4]. Immiscible alloys, containing a stable or metastable miscibility gap in the liquid state, undergo a liquid–liquid phase separation during the solidification process, i.e., a homogeneous liquid decomposes into two immiscible liquids [3]. Under normal circumstances, since the two immiscible liquids have different enrichments relative to the components, there is a large difference in density between them. Hence, immiscible alloys tend to form severe gravity segregation and even component stratification under conventional solidification condition, resulting in the loss of application value. Therefore, if the minority phase is dispersed in the matrix by appropriate methods, the special physical and mechanical properties they exhibit will have broad application prospects. Thus, it is important to obtain a uniform structure of immiscible alloys.

Al–Bi–Sn monotectic alloys are characterized by microstructures formed by immiscible phases with the minority phase dispersed throughout the Al matrix. The dispersed minority phase can provide appropriate tribological characteristics acting as a solid lubricant, while the matrix provides required structural integrity [5]. To effectively control the distribution of the minority phase of Al–Bi–Sn alloy, the solidification mechanism of immiscible alloys must be understood. However, little literature has discussed the solidification mechanism. In recent years, experimental studies on factors influencing the structure of solidification have been conducted, including composition [6, 7], temperature gradient [8], the cooling rate [9], and the degree of undercooling [10]. As for Al–Bi–Sn immiscible alloys, the minority phase with higher density tends to move downward under gravity conditions. What' more, the thermal Marangoni motion rate of the minority phase will be affected by the temperature gradient. Cooling rate is an important factor affecting the minority phase distribution, which determines directly the minority phase droplets growth, roughening, moving, and the duration separated from the matrix phase [11]. Therefore, under different cooling conditions, the morphology and distribution of

https://doi.org/10.1557/jmr.2019.202 Published online by Cambridge University Press

© Materials Research Society 2019

minority phase droplets are different and then can be controlled. However, few studies were researched about the effect of cooling rate on the morphology of the minority phase.

In this paper, a ternary immiscible alloy with the composition of $Al_{70}Bi_{10}Sn_{20}$ (at.%) was prepared, where the alloy composition was designed to fall into the stable miscibility gap in the liquid state. What's more, temperature range of stable miscibility gap of this composition is about 200 °C, which is benefit to study the process of liquid phase separation. Three different cooling conditions were conducted to investigate the structural evolution. By this means, the formation and evolution of the microstructure of this component melt under different solidification conditions were studied. The corresponding solidification mechanism was further discussed and uncovered.

Results

Morphology and microstructure of Al–Bi–Sn alloy under conventional solidification condition

Figure 1(a) shows the macroscopic solidification structure of the $Al_{70}Bi_{10}Sn_{20}$ ingot cast into graphite mold. A serious spatial phase separation appears, i.e., the upper is the Al-rich region with a lower density and the bottom is the Bi–Sn-rich region. In addition, a clear boundary can be observed between the Al-rich and Bi–Sn-rich regions, as shown in Fig. 1(c). A portion of the Bi–Sn-rich phase distributes in the upper Al-rich region [Fig. 1(b)], and a considerable amount of Al-rich phase distributes in the lower Bi–Sn-rich region [Fig. 1(d)].

Generally, there are mainly two different morphology types of Bi–Sn-rich phase in the Al-rich region, i.e., a spherical type within the α-Al grain and continuous net structure distributed in the α-Al interdendrites (Fig. 2). It can be ascertained that the Bi–Sn-rich spherical or ellipsoidal droplets in the Al-rich region are the product of the liquid–liquid phase separation. Accompanied by the solidification of α-Al phase with the high liquidus temperature, the Bi–Sn-rich droplets are frozen in the Al matrix during the solidification process. Under the action of interfacial tension, the Bi–Sn-rich droplets maintain a spherical morphology. Another Bi–Sn-rich phase distributes in the α-Al interdendrites, forming a continuous net structure, which is the product of monotectic reaction [11].

Figure 3(a) is the further enlarged structure of the Bi–Sn-rich region in the lower layer of the sample. It can be observed that the lamellar structure is distributed as a matrix in the Bi–Sn-rich region, which was also found in the previous study [12]. Nevertheless, the corresponding formation reason has rarely been reported. The map scanning result shows that the lamellar structure consists of Bi and Sn [Figs. 3(d)–3(f)]. To identify the formation of the lamellar structure, differential scanning calorimeter (DSC) test was carried out. Figure 4(a) shows the DSC result of the sample taken from the Bi–Sn-rich region of the $Al_{70}Bi_{10}Sn_{20}$ alloy ingot solidified in the graphite mold. During heating and cooling process, the endothermic (146.50 °C) and exothermic (127.89 °C) peaks can be clearly observed, which is approximately close to the Bi–Sn eutectic

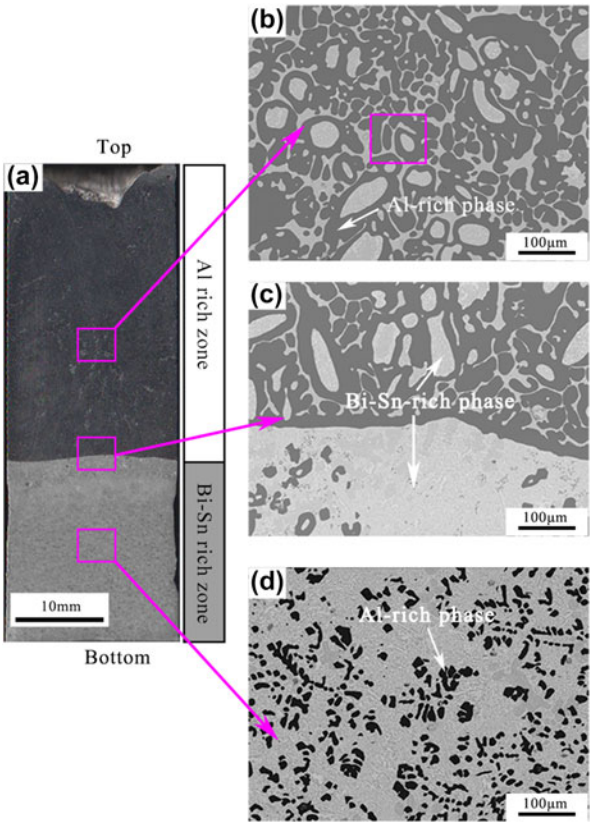


Figure 1: (a) Total longitudinal section view of $Al_{70}Bi_{10}Sn_{20}$ alloy cast into a graphite mold at 1000 °C. (b)–(d) Enlarged backscattered electron images of the corresponding rectangle region in (a).

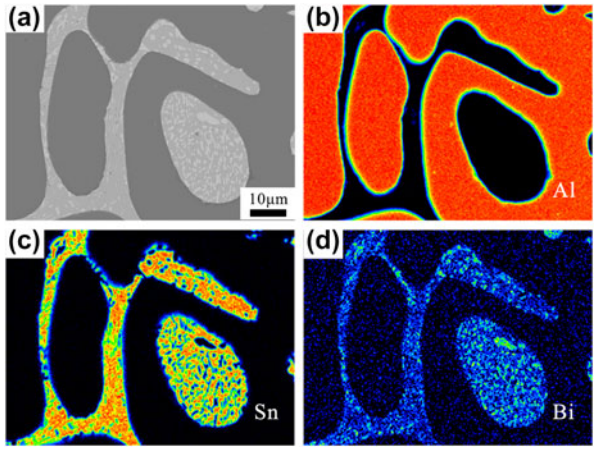


Figure 2: (a) Backscattered electron image of the enlarged rectangle region in Fig. 1(b). (b)–(d) Map scanning of (a) by electron probe micro-analyzer.

https://doi.org/10.1557/jmr.2019.202 Published online by Cambridge University Press

© Materials Research Society 2019

reaction temperature (140.69 °C) [13, 14]. However, two distinct types of Bi–Sn lamellar structures [Fig. 3(a)] are observed in the Bi–Sn-rich region, namely, the discontinuous lamellar structure [Fig. 3(b)] and the regular lamellar pattern like the shape of "fishbone" [Fig. 3(c)]. To further ascertain whether the lamellar structure is the production of eutectic structure or discontinuous precipitation, the as-taken Bi–Sn-rich sample was solution treated at 130 °C, which is below the eutectic temperature for 5 h. Interestingly, the lamellar structure barely changes as shown in Fig. 4(b), which further demonstrates that it is the production of eutectic reaction. In addition, it can be observed from the energy-dispersive spectroscopy (EDS) pattern of the rectangle region in Fig. 5 that Bi and Sn solutes do not exist in the primary α-Al phase, demonstrating that both Bi and Sn elements have negligible solid solubility in the Al-rich matrix.

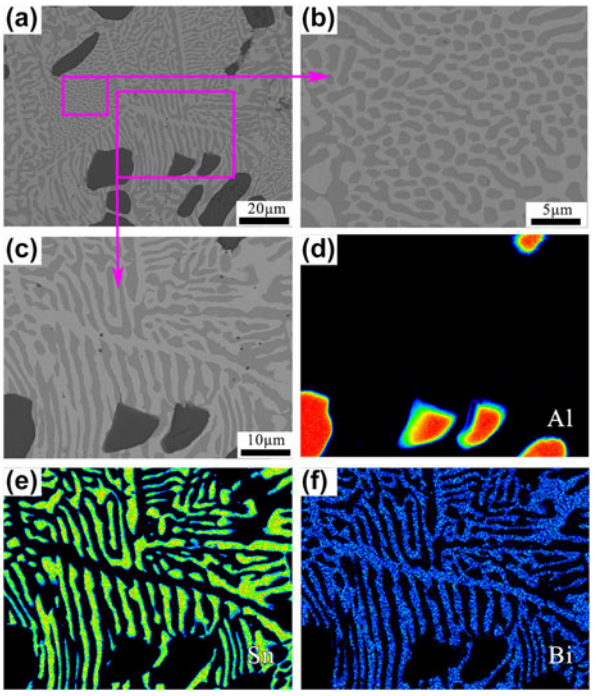


Figure 3: (a) Backscattered electron (BSE) image of Bi–Sn-rich region of the $Al_{70}Bi_{10}Sn_{20}$ alloy cast into a graphite mold. (b) and (c) Enlarged BSE images of the corresponding rectangle region in (a). (d)–(f) Map scanning of (c) by electron probe micro-analyzer.

Solidification microstructure evolution of Al–Bi–Sn alloy at different cooling rates

Based on the above experimental results, it is found that the gravity segregation leads to serious phase separation at a low cooling rate. To further study the solidification mechanism of the immiscible alloy, the rapid cooling in copper mold and water quenching experiments were carried out.

Figure 6 shows the microstructures of $Al_{70}Bi_{10}Sn_{20}$ alloy solidified in the copper mold. It can be seen that the samples at different cooling rates present various morphology. Figure 6(a) presents the solidification microstructure solidified at a cooling rate of about 400 °C/s. A significant gravity segregation takes place. Macroscopically, the sample exhibits a distinct layered microstructure, in which the upper and bottom regions are Al-rich and Bi–Sn-rich structures, respectively. Meanwhile, just above the interface of the two regions, there are many tadpole-like Bi–Sn-rich droplets, which are elongated along the vertical direction. It is generally accepted that the nucleation of the minority phase during liquid–liquid separation process can be considered as uniform nucleation [3]. Thus, the nucleation rate in each position should be approximately spatially identical. The newly generated Bi–Sn-rich droplets near the bottom can easily coagulate and settle down under the driving of gravity, which ultimately results in the settled Bi–Sn-rich region. For other generated Bi–Sn-rich droplets away from the bottom of mold, they have no enough time to sink to the bottom, instead they are trapped in the middle of alloy eventually. In addition, these Bi–Sn-rich droplets tend to collide and coalesce during solidification process [15]; meanwhile, they migrate downward due to the influence of gravity [15, 16]. Thus, the Bi–Sn-rich droplets elongated in the vertical direction indicate the trend of

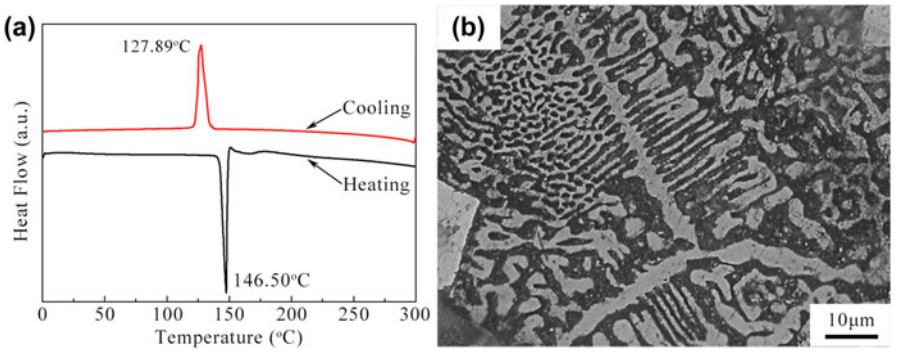


Figure 4: (a) DSC curves of Bi–Sn-rich region of the $Al_{70}Bi_{10}Sn_{20}$ alloy cast into a graphite mold. (b) Backscattered electron image of Bi–Sn-rich region after solution treatment at 130 °C for 5 h.

https://doi.org/10.1557/jmr.2019.202 Published online by Cambridge University Press

© Materials Research Society 2019

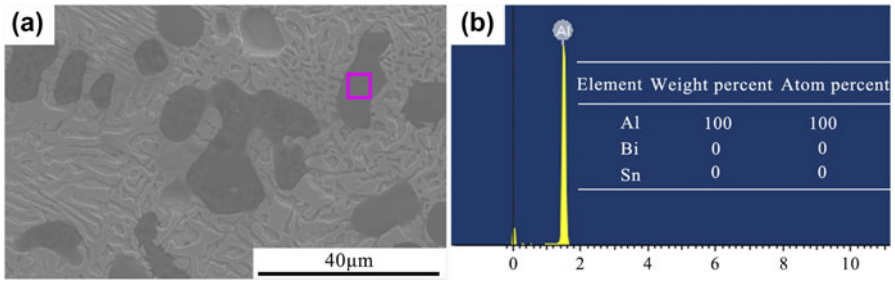


Figure 5: (a) Scanning electron microscopic image of the Bi–Sn-rich region. (b) EDS result of the rectangle region in (a).

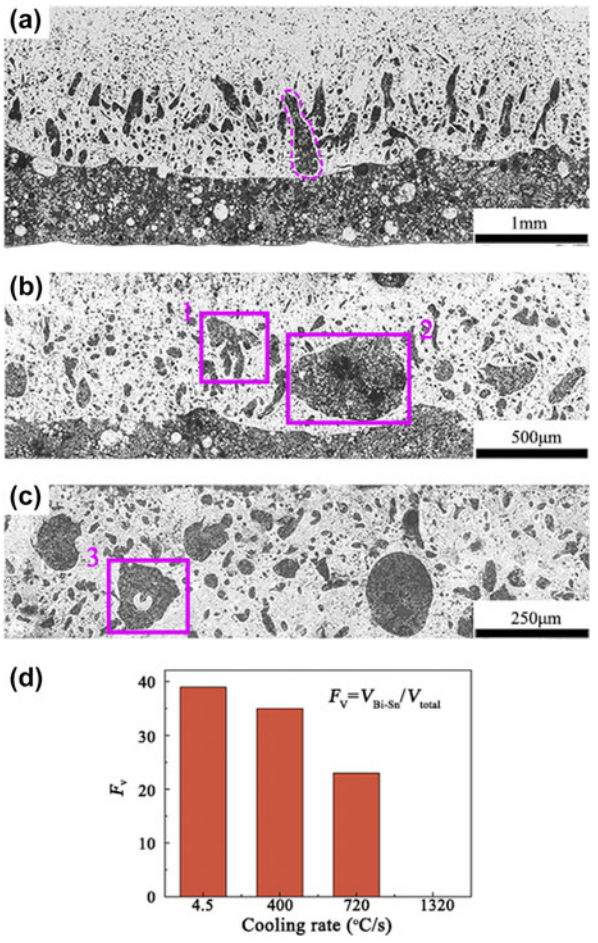


Figure 6: (a)–(c) Microstructure of $Al_{70}Bi_{10}Sn_{20}$ alloys poured into the copper mold at different cooling rates: (a) 400 °C/s, (b) 720 °C/s, and (c) 1320 °C/s. (d) The volume fractions of the Bi–Sn-rich region (F_V) of the alloy with different cooling rates.

downward movement. It is worth noting that two ellipsoidal Bi–Sn-rich droplets in the dashed box in Fig. 6(a) are frozen in the process of coalescing and eventually solidify in morphology of the tadpole.

For the solidification microstructure of $Al_{70}Bi_{10}Sn_{20}$ solidified at a cooling rate of about 720 °C/s, it can be seen in Fig. 6(b) that a large part of the Bi–Sn-rich phase still concentrates at the bottom, similar to that observed in Fig. 6(a). Meanwhile, another part of the Bi–Sn-rich phase is observed to solidify in the middle. It should be noted that several Bi–Sn-rich droplets with different sizes are merging together, while they do not complete the coalescence due to the large cooling rate [as can be seen in the rectangle 1 in Fig. 6(b)]. In addition, a large Bi–Sn-rich droplet is frozen in the Al-rich region [as highlighted by the rectangle 2 in Fig. 6(b)]. As the cooling rate further increases to about 1320 °C/s, a typical layered structure is not formed in the sample, instead several large Bi–Sn-rich droplets are distributed in the matrix [see Fig. 6(c)]. Interestingly, a special structure is formed that the Bi–Sn-rich phase encases the Al-rich phase, because the Bi–Sn-rich droplet envelops the Al-rich droplet during the growth and coagulation process [as highlighted by the rectangle 3 in Fig. 6(c)].

To determine the degree of spatial phase separation, the volume fraction of the bottom segregated Bi–Sn-rich region (F_V) is estimated. F_V is defined as follows:

$$F_V = V_{Bi-Sn}/V_{total} \quad , \tag{1}$$

where V_{Bi-Sn} denotes the volume of the bottom Bi–Sn-rich region and V_{total} stands for the total volume of the alloy sample. Figure 6(d) plots the degree of spatial phase separation versus cooling rate. F_V of the samples with cooling rates of 4.5 °C/s, 400 °C/s, 720 °C/s, and 1320 °C/s are 38.9%, 34.8%, 23.1%, and 0%, respectively. The result shows that the volume fraction of the bulk segregated Bi–Sn-rich region shows a significant decrease with increasing cooling rate. It is concluded that increasing the cooling rate can significantly suppress the spatial phase segregation.

It is seen from Fig. 6 that the microstructure significantly changes with the increase in the cooling rate. Meanwhile, the degree of segregation can be greatly inhibited. Thus, to further investigate the microstructure of Al–Bi–Sn alloy with a high cooling condition, water quenching experiment was carried out. As estimated that the cooling rate is about 2900 °C/s under this condition. The microstructure of the $Al_{70}Bi_{10}Sn_{20}$ alloy, which is cast into water directly, is presented in Fig. 7. Unlike the above-mentioned samples solidified in the copper mold, the sample does not exhibit spatial phase separation

https://doi.org/10.1557/jmr.2019.202 Published online by Cambridge University Press

© Materials Research Society 2019

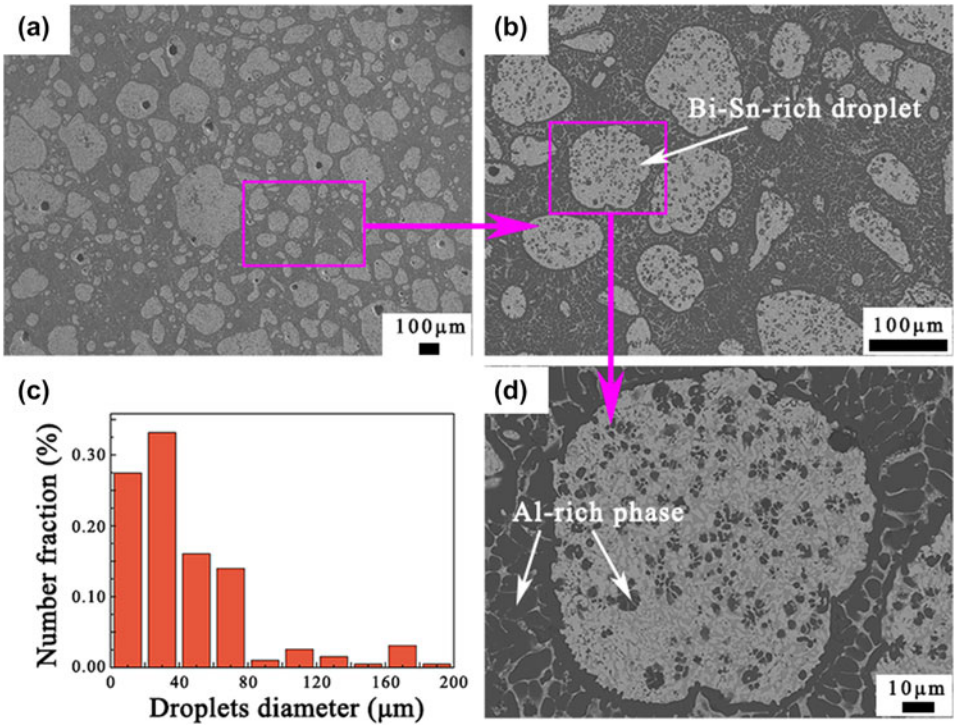


Figure 7: (a) Microstructure of $Al_{70}Bi_{10}Sn_{20}$ alloy solidified in water. (b) Enlarged image of (a). (c) 2D diameter distribution of the minority phase droplets in the $Al_{70}Bi_{10}Sn_{20}$ alloy solidified in water. (d) Further enlarged image of (b).

from a macro perspective [see Figs. 7(a) and 7(b)]. Figure 7(c) shows the statistical result of droplet size. Compared with the sample solidified at the cooling rate of 1320 °C/s, the number of Bi–Sn-rich droplets is larger and the size is smaller. At such extremely high cooling rate, the minority phase is dispersed relatively evenly in the matrix. Figure 7(d) shows the presence of some secondary Al grains distributed in the Bi–Sn-rich droplets.

Discussion

According to the previous studies, the solidification process of $Al_{70}Bi_{10}Sn_{20}$ alloy can be summarized: when the homogeneous melt is undercooled into the miscibility gap, the liquid–liquid separation takes place, i.e., $L \rightarrow L_1$ (Al-rich) + L_2 (Bi–Sn-rich). Then, the minority phase nucleates preferentially in a form of dispersed liquid globules [4]. Subsequently, the minority phase droplets mainly grow by the multiple mechanisms, such as diffusion-controlled growth, Brownian motion, Marangoni motion, and Stokes sedimentation. When the temperature decreases to T_m, the monotectic reaction occurs: $L_1 \rightarrow S$ (Al) + L_2, followed by the Bi–Sn eutectic reaction [17].

Thus, the schematic illustration of the solidification path of $Al_{70}Bi_{10}Sn_{20}$ alloy under different cooling conditions is shown in Fig. 8. In the liquid–liquid phase separation process of $Al_{70}Bi_{10}Sn_{20}$ alloy melt, the minority phase droplets have undergone processes such as nucleation, diffusion-controlled growth Brownian motion, Ostwald ripening, collision, Stokes sedimentation and Marangoni migration [18, 19, 20]. The Marangoni migration and Stokes sedimentation are the main reason for the macrosegregation of the immiscible alloys. The Stokes sedimentation velocity V_s and Marangoni migration velocity V_m of the minority phase droplets with radius r in the liquid alloy are described in the following equations [21, 22]:

$$V_m \approx \frac{-2r}{3(2\eta_1 + 3\eta_2)} \cdot \frac{\partial \sigma}{\partial T} \cdot \frac{\partial T}{\partial x} \quad , \tag{2}$$

$$V_s \approx \frac{2}{3} \frac{(\rho_2 - \rho_1)(\eta_2 + \eta_1)g}{\eta_1(2\eta_1 + 3\eta_2)} \cdot r^2 \quad , \tag{3}$$

where η_1 and η_2 are the viscosities of the matrix and minor droplet, respectively; r is the radius of the minor droplet; σ is the interfacial energy; x is the distance; ρ_1 and ρ_2 are the densities of the matrix and minor droplet, respectively; and g is the gravity coefficient.

According to Eqs. (2) and (3), V_m is influenced by σ and V_s is related to g. So the minority phase droplets will move toward the high-temperature center driven by the Marangoni effect and move downward driven by Stokes motion. Furthermore, V_m is proportional to r, whereas V_s is proportional to r^2, indicating that V_s increases quicker with r than V_m. The motion

https://doi.org/10.1557/jmr.2019.202 Published online by Cambridge University Press

© Materials Research Society 2019

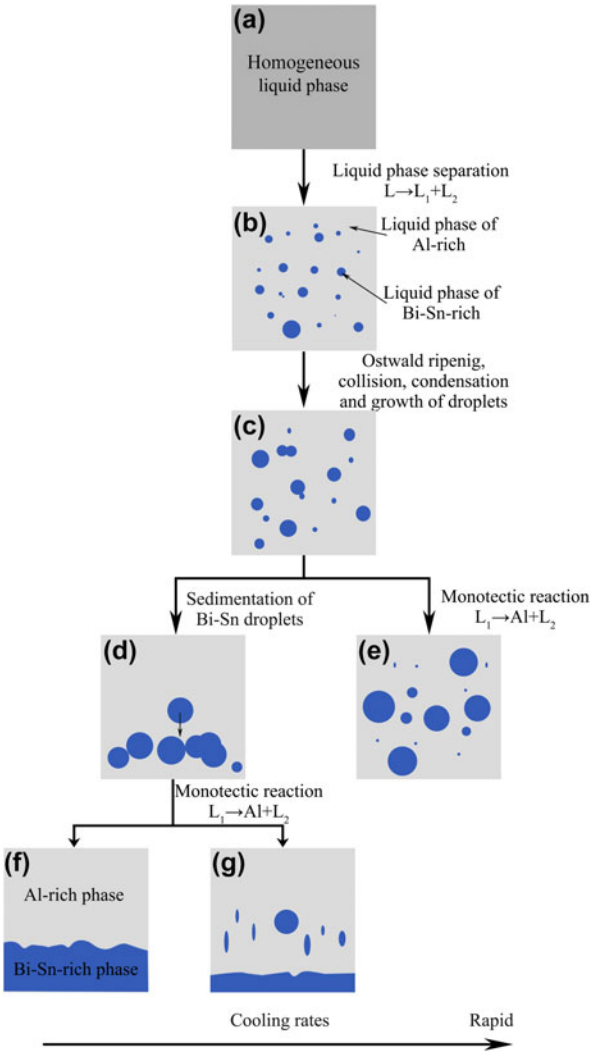


Figure 8: Schematic illustration of the solidification process of $Al_{70}Bi_{10}Sn_{20}$ alloy solidified under different cooling conditions (a–g) correspond to different stages during solidification process.

direction of the minority phase droplets is determined by the combined velocity of V_m and V_s [23]. Therefore, in the initial period of liquid–liquid phase separation, V_m is much larger than V_s because of the small size of droplets and the large temperature gradient [9, 20]. Because the inner region of the as-cast sample has a higher temperature than the surface, the small droplets move toward the inner region by the thermal Marangoni migration, accompanying the growth by collision and coagulation during movement. In addition, gravity-induced Stokes velocity (V_s) direction of the Bi–Sn-rich droplets is always downward. With the proceeding of cooling, the temperature gradient decreases and the size of minority droplets increases. The effect of gravity becomes increasingly pronounced accordingly. Obviously, the cooling rate determines the duration in which the alloy melt remains liquid, which is an important factor in determining the impact of gravity.

Different solidification structures are formed under different cooling conditions. When the cooling rate is 4.5 °C/s, the time period of collision and growth of the minority phase droplets is long that lots of large minority phase droplets will be formed during liquid phase separation process [Fig. 8(d)]. Under this condition, the Stokes migration plays a major role, and eventually a serious spatial separation structure is formed [Fig. 8(f)]. When the cooling rate is increased to 400 °C/s, the volume fraction of the bottom-settled Bi–Sn-rich region reduces due to the shorter migration time. A large part of the Bi–Sn-rich phase droplets is deposited to the bottom and another part of the minority phase is frozen in the Al-rich region [Fig. 8(g)]. When the cooling rate reaches 720 °C/s, the bulk separated Bi–Sn-rich phase frozen in the Al-rich region is caused by the coaction between Stokes sedimentation and Marangoni migration. The newly nucleated Bi–Sn-rich droplets near the bottom coagulate and deposit due to the Stokes motion. It is worth mentioning that the degree of spatial phase separation greatly decreases with increasing cooling rate. When the cooling rate reaches from 1320 to 2900 °C/s, spatial separation disappears, instead the minority phase droplets are evenly distributed in the Al-rich matrix to some extent [Fig. 8(e)].

In general, the cooling rate has a significant effect on the microstructure of Al–Bi–Sn alloy. When the alloy melt solidifies at a slower cooling rate, significant spatial phase separation occurs. As the cooling rate increases, the microstructure of the alloy can be tuned and the degree of phase separation is to a great extent suppressed. Therefore, the present research offers a new set into the method to tailor the microstructure of the Al–Bi–Sn immiscible alloy.

Conclusions

In this study, the effect of cooling rate on the microstructure of the $Al_{70}Bi_{10}Sn_{20}$ alloy, which is located in the immiscible region, was studied by the designed three different cooling conditions. The result shows that cooling rate has a significant effect on the morphology and distribution of the minority phase of $Al_{70}Bi_{10}Sn_{20}$ alloy. Under conventional solidification conditions, because of the different density between minority phase and matrix, macrosegregation is inevitable, or even forms an obvious stratification. As the cooling rate increases, the degree of spatial phase separation decreases, and more minority phase droplets are frozen in the Al-rich matrix. When the cooling rate reaches 2900 °C/s, the minority phase droplets are evenly distributed in the Al-rich matrix to some extent. Therefore, the formation of the microstructure of the $Al_{70}Bi_{10}Sn_{20}$ ternary immiscible alloy can be controlled by adjusting the solidification condition.

https://doi.org/10.1557/jmr.2019.202 Published online by Cambridge University Press

© Materials Research Society 2019

Experimental procedure

Preparation of the $Al_{70}Bi_{10}Sn_{20}$ alloy

The alloy ingot with the nominal composition of Al–10 at.% Bi–20 at.% Sn was prepared by pure Al (99.85 wt%), Bi (99.99 wt%), and Sn (99.99 wt%) through medium frequency induction melting. The pseudo-binary diagram is depicted in Fig. 9 relative to a parameterized concentration of 20 at.% Sn [24]. The location of the experimental alloy was in the liquid miscibility gap, indicating that the solidification path of the experimental alloy would undergo the liquid–liquid separation process. The pure Al, Bi, and Sn were melted in a graphite crucible. Then, the alloy melt was mechanically stirred during the smelting process to make sure the sufficient mixing of all components for homogeneity. After induction melting and holding for 10 min at 1000 °C, the alloy melt was cast under different conditions.

Solidification at different cooling rates

To obtain different solidification rates, three kinds of solidification processes were adopted. The following is the experimental procedure:

(i) Conventional solidification process in the graphite mold. The melt was cast into a graphite crucible with an inner diameter of 20 mm and a depth of 60 mm. The graphite crucible parceled by two layers of insulation asbestos was preheated to 700 °C. The cooling rate of this sample was 4.5 °C/s, according to the measured cooling curve by using the K-type thermocouple.

(ii) Copper mold rapid cooling experiment. The melt was rapidly cast into a copper plate mold with the orthogonal groove and covered immediately by another copper plate in the meantime. Three prepared samples were in the shape of lamellae with dimensions of 10 × 8 × 2.58 mm, 10 × 8 × 0.98 mm, and 10 × 8 × 0.37 mm. For this condition, the cooling rate $\dot{T}$ can be estimated by an empirical equation as follows [25].

$$\dot{T} = KZ^n \quad , \tag{4}$$

where K and n are constants dependent on the material and the geometry of the mold. For this experiment, the parameters K = 715 and n = −0.619 are estimated [26]. Hence, it was estimated that the cooling rates were about 400 °C/s, 720 °C/s, and 1320 °C/s in the copper plate molds with the sample thicknesses of 2.58 mm, 0.98 mm, and 0.37 mm, respectively.

(iii) Water quenching experiment. Some spherical samples were prepared by quenching the melt into water directly after holding for 10 min at 1000 °C in medium frequency induction furnace. Because of the small size of liquid alloy spheres and dispersion in the water, it is difficult to measure the temperature change in the real-time manner. The heat conduction and heat convection processes were considered when alloy droplets descended in water [8]. The cooling rate R_c was calculated by the Newtonian model as follows [27, 28]:

$$R_c = \left|\frac{dT}{dt}\right| = \frac{6}{\rho_d C_p D} h(T - T)_l \quad , \tag{5}$$

with

$$h = \frac{k_l}{D}\left(2 + 0.3\mathrm{Pr}^{0.33}\mathrm{Re}^{0.6}\right) \quad , \tag{6}$$

$$\mathrm{Pr} = \frac{C_p \mu}{k_l},\ \mathrm{Re} = \frac{\rho_l D V}{\mu} \quad , \tag{7}$$

where ρ_d is the density of alloy droplets, C_p is the specific heat, D is the diameter of alloy droplets, h is the heat transfer coefficient of water, T is the casting temperature, T_l is the temperature of water, k_l is the thermal conductivity of water, P_r is Prandtl number, Re is Reynolds number, μ is the dynamic viscosity of water, and ρ_l is the density of water. The corresponding parameters are presented in Table I.

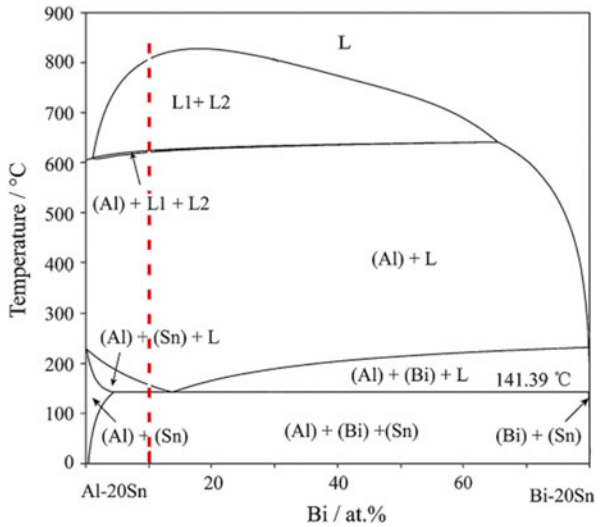


Figure 9: The calculated vertical sections of the Al–Bi–Sn ternary system with 20 at.% Sn.

TABLE I: The parameters used in the calculation.

Parameters	Value	References
Density of droplet, ρ_d (kg/m^3)	4719	Measured
Specific heat of liquid alloy, C_p [J/(kg K)]	671	[29]
Thermal conductivity of water, k_g [W/(m K)]	0.599	...
Viscosity of water, μ [kg/(m s)]	1.005×10^{-3}	...

https://doi.org/10.1557/jmr.2019.202 Published online by Cambridge University Press

© Materials Research Society 2019

When $D = 5$ mm, it is estimated that the cooling rate R_c was about 2900 °C/s.

Characterization

To reveal the solidification behavior of immiscible $Al_{70}Bi_{10}Sn_{20}$ alloy at different cooling rates, the samples were ground, polished, and etched for morphology observation and phase composition analysis. The samples were etched by a solution containing 5 g $FeCl_3$, 5 mL HCl, and 95 mL C_2H_5OH. Microstructures were examined by an optical microscope (Japan, Olympus GX51), a scanning electron microscope (Germany, Zeiss supra 55) equipped with an EDS (UK, Oxford INCA X-ACT), and an electron probe micro-analyzer (Japan, JXA-8530F PLUS). The samples used for composition analysis were not etched. Phase transformation behavior was investigated using DSC (STA 449C) at a scan rate of 10 °C/min from room temperature to 300 °C (Germany, NETZSCHS—TA449C).

Acknowledgments

The authors gratefully acknowledge the supports of National Key Research and Development Program of China (Nos. 2016YFB0301303 and 2017YFA0403800) and the National Natural Science Foundation of China (Nos. 51771040, 51501028, 51690163, and 51525401).

References

1. **A. Inoue, N. Yano, K. Matsuzaki, and T. Masumoto**: Microstructure and superconducting properties of melt-quenched insoluble Al–Pb and Al–Pb–Bi alloys. *J. Mater. Sci.* **22**, 123 (1987).
2. **I. Kaban, M. Köhler, L. Ratke, W. Hoyer, N. Mattern, J. Eckert, and A.L. Greer**: Interfacial tension, wetting and nucleation in Al–Bi and Al–Pb monotectic alloys. *Acta Mater.* **59**, 6880 (2011).
3. **L. Ratke and S. Diefenbach**: Liquid immiscible alloys. *Mater. Sci. Eng., R* **15**, 263 (1995).
4. **R. Dai, J.F. Zhang, S.G. Zhang, and J.G. Li**: Liquid immiscibility and core–shell morphology formation in ternary Al–Bi–Sn alloys. *Mater. Charact.* **81**, 49 (2013).
5. **T.A. Costa, E.S. Freitas, M. Dias, C. Brito, N. Cheung, and A. Garcia**: Monotectic Al–Bi–Sn alloys directionally solidified: Effects of Bi content, growth rate and cooling rate on the microstructural evolution and hardness. *J. Alloys Compd.* **653**, 243 (2015).
6. **H.R. Kotadia, A. Das, E. Doernberg, and R. Schmid-Fetzer**: A comparative study of ternary Al–Sn–Cu immiscible alloys prepared by conventional casting and casting under high-intensity ultrasonic irradiation. *Mater. Chem. Phys.* **131**, 241 (2011).
7. **R. Dai, S. Zhang, X. Guo, and J. Li**: Formation of core-type microstructure in Al–Bi monotectic alloys. *Mater. Lett.* **65**, 322 (2011).
8. **W.Q. Lu, S.G. Zhang, and J.G. Li**: Macrosegregation driven by movement of minor phase in $(Al_{0.345}Bi_{0.655})_{90}Sn_{10}$ immiscible alloy. *Appl. Phys. A* **117**, 787 (2014).
9. **R. Dai, S. Zhang, Y. Li, X. Guo, and J. Li**: Phase separation and formation of core-type microstructure of Al–65.5 mass% Bi immiscible alloys. *J. Alloys Compd.* **509**, 2289 (2011).
10. **L. Ning**: Investigation on the phase separation in undercooled Cu–Fe melts. *J. Non-Cryst. Solids* **358**, 196 (2012).
11. **C. Wu, M. Li, P. Jia, R. Liu, S. Cui, and H. Geng**: Solidification of immiscible $Al_{75}Bi_9Sn_{16}$ alloy with different cooling rates. *J. Alloys Compd.* **688**, 18 (2016).
12. **M. Li, Y. Zhang, W. Chen, and H. Geng**: Effect of liquid–liquid structure transition on solidification of $Sn_{57}Bi_{43}$ alloy. *Appl. Phys. A* **122**, 1 (2016).
13. **B.L. Silva, G. Reinhart, H. Nguyen-Thi, N. Mangelinck-Noël, A. Garcia, and J.E. Spinelli**: Microstructural development and mechanical properties of a near-eutectic directionally solidified Sn–Bi solder alloy. *Mater. Charact.* **107**, 43 (2015).
14. **M. Li, H. Geng, L. Fang, Z. Min, R. Liu, and S. Lu**: Discontinuous structural phase transition of Sn–Bi melts. *J. Mol. Liq.* **204**, 27 (2015).
15. **S. Liu, J. Jie, B. Dong, Z. Guo, T. Wang, and T. Li**: Novel insight into evolution mechanism of second liquid–liquid phase separation in metastable immiscible Cu–Fe alloy. *Mater. Des.* **156**, 71 (2018).
16. **R.P. Shi, Y. Wang, C.P. Wang, and X.J. Liu**: Self-organization of core–shell and core–shell-corona structures in small liquid droplets. *Appl. Phys. Lett.* **98**, 15 (2011).
17. **W. Lin, S. Li, B. Lin, W. Di, and D. Zhao**: Liquid–liquid phase separation and solidification behavior of Al–Bi–Sn monotectic alloy. *J. Mol. Liq.* **254**, 333 (2018).
18. **D. Zhao, L. Bo, L. Wang, and S. Li**: Liquid–liquid phase separation and core–shell structure of ternary Al–In–Sn immiscible alloys. *Mater. Res. Express* **5**, 046508 (2018).
19. **S. Liu, J. Jie, J. Zhang, P. Wang, T. Wang, T. Li, and G. Yin**: A surface energy driven dissolution model for immiscible Cu–Fe alloy. *J. Mol. Liq.* **261**, 232 (2018).
20. **P. Jia, Y. Li, X. Hu, J. Zhang, X. Teng, D. Zhao, Q. Chen, M. Zuo, Q. Liu, and C. Yang**: Formulation of Al–Bi–Sn immiscible alloys versus the solidification behaviors and structures. *J. Mater. Sci.* **54**, 4384 (2019).
21. **E. Lavernia, R. Ghanshyam, and N. Grant**: Liquid dynamic compaction of a rapidly solidified high strength aluminum alloy. *Int. J. Powder Metall.* **22**, 9 (1986).
22. **C.P. Wang, X.J. Liu, I. Ohnuma, R. Kainuma, and K. Ishida**: Formation of immiscible alloy powders with egg-type microstructure. *Science* **297**, 990 (2002).
23. **W.L. Wang, Z.Q. Li, and B. Wei**: Macrosegregation pattern and microstructure feature of ternary Fe–Sn–Si immiscible alloy solidified under free fall condition. *Acta Mater.* **59**, 5482 (2011).
24. **H.X. Liu, C.P. Wang, Y. Yu, X.J. Liu, Y. Takaku, I. Ohnuma, R. Kainuma, and K. Ishida**: Experimental investigation and

https://doi.org/10.1557/jmr.2019.202 Published online by Cambridge University Press

© Materials Research Society 2019

thermodynamic calculation of the phase equilibria in the Al–Bi–Sn ternary system. *J. Phase Equilib. Diffus.* **33**, 9 (2012).

25. **S. Curiotto, N.H. Pryds, E. Johnson, and L. Battezzati**: Effect of cooling rate on the solidification of $Cu_{58}Co_{42}$. *Mater. Sci. Eng., A* **449**, 644 (2007).
26. **S. Liu, J. Jie, Z. Guo, G. Yin, T. Wang, and T. Li**: Solidification microstructure evolution and its corresponding mechanism of metastable immiscible $Cu_{80}Fe_{20}$ alloy with different cooling conditions. *J. Alloys Compd.* **742**, 99 (2018).
27. **Y. Ruan, Q.Q. Wang, S.Y. Chang, and B. Wei**: Structural evolution and micromechanical properties of ternary AlAgGe alloy solidified under microgravity condition. *Acta Mater.* **141**, 456 (2017).
28. **H.Z. Zhu, Y. Ruan, Q.Q. Gu, N. Yan, and F.P. Dai**: Rapid solidification mechanism and magnetic properties of Ni–Fe–Ti alloy prepared in drop tube. *Acta Phys. Sin.* **66**, 138101 (2017).
29. **J.F. Zhang, Y.J. Wang, W.Q. Lu, S.G. Zhang, and J.G. Li**: The core shell structure of $Al_{70}Bi_{11}Sn_{19}$ immiscible alloy particles. *Acta Metall. Sin.* **29**, 457 (2013).

https://doi.org/10.1557/jmr.2019.202 Published online by Cambridge University Press

© Materials Research Society 2019